symmetry

MDPI

Article

The Relationship between Cardiomyocyte Action Potentials and Ion Concentrations: Machine Learning Prediction Modeling and Analysis of Spontaneous Spiral Wave Generation Mechanisms

Jing Bai [1,2], Chunfu Zhang [1,2], Yanchun Liang [3,*], Adriano Tavares [2,*], Lidong Wang [1,*], Xue Gu [2] and Ziyao Meng [2]

[1] School of Data Science, Zhuhai College of Science and Technology, Zhuhai 519041, China; baijing@zcst.edu.cn (J.B.); cfzhang@zcst.edu.cn (C.Z.)
[2] Department of Industrial Electronics, University of Minho, 4800-058 Guimaraes, Portugal; id9267@alunos.uminho.pt (X.G.); id9272@alunos.uminho.pt (Z.M.)
[3] School of Computer Science, Zhuhai College of Science and Technology, Zhuhai 519041, China
* Correspondence: ycliang@jlu.edu.cn (Y.L.); atavares@dei.uminho.pt (A.T.); wld@zcst.edu.cn (L.W.)

Abstract: The changes in cardiomyocyte action potentials are related to variations in intra- and extracellular ion concentrations. Abnormal ion concentrations can lead to irregular action potentials, subsequently affecting wave propagation in myocardial tissue and potentially resulting in the formation of spiral waves. Therefore, timely monitoring of ion concentration changes is essential. This study presents a novel machine learning classification model that predicts ion concentration changes based on action potential variation data. We conducted simulations using a single-cell model, generating a dataset of 850 action potential variations corresponding to different ion concentration changes. The model demonstrated excellent predictive performance, achieving an accuracy of 0.988 on the test set. Additionally, the causes of spontaneous spiral wave generation in the heart are insufficiently studied. This study presents a new mechanism whereby changes in extracellular potassium ion concentration leads to the spontaneous generation of spiral waves. By constructing composite myocardial tissue containing both myocardial and fibroblast cells, we observed that variations in extracellular potassium ion concentration can either trigger or inhibit cardiomyocyte excitation. We developed three tissue structures, and by appropriately adjusting the extracellular potassium ion concentration, we observed the spontaneous generation of single spiral waves, symmetrical spiral wave pairs, and asymmetrical double spiral waves.

Keywords: artificial neural networks; ion concentration; action potential; spiral wave; cardiomyocytes; fibroblasts

check for updates

Citation: Bai, J.; Zhang, C.; Liang, Y.; Tavares, A.; Wang, L.; Gu, X.; Meng, Z. The Relationship between Cardiomyocyte Action Potentials and Ion Concentrations: Machine Learning Prediction Modeling and Analysis of Spontaneous Spiral Wave Generation Mechanisms. *Symmetry* **2024**, *16*, 1136. https://doi.org/10.3390/sym16091136

Academic Editor: Sergei D. Odintsov

Received: 4 July 2024
Revised: 29 August 2024
Accepted: 29 August 2024
Published: 2 September 2024

Copyright: © 2024 by the authors. Licensee MDPI, Basel, Switzerland. This article is an open access article distributed under the terms and conditions of the Creative Commons Attribution (CC BY) license (https://creativecommons.org/licenses/by/4.0/).

1. Introduction

The heart is the powerhouse of the human circulatory system, functioning to propel blood throughout the body via contraction and relaxation. Cardiac contraction is triggered by electrical impulses originating from the sinoatrial node, which then propagate through the atria and ventricles. Upon receiving these electrical impulses, cardiac muscle cells rapidly depolarize, generating action potentials. Action potentials are the physiological basis for muscle contraction and serve as objective markers for the conduction in excitable cells.

The regulation of cardiac function heavily relies on the action potential of cardiomyocytes, which is essential for maintaining a normal heart rhythm and effective cardiac contraction [1]. Action potentials in cardiomyocytes are facilitated by changes in ion currents within the cells, driven by specific ion concentrations inside and outside the cell membrane. Any deviation in these ion concentrations can lead to abnormal ion currents, causing distorted action potentials [2,3]. These irregular electrical activities present as

arrhythmias on an electrocardiogram, such as heart block, tachycardia, and ventricular fibrillation, potentially compromising cardiac function and posing life-threatening risks [4–6]. Therefore, it is crucial to monitor changes in ion concentrations within cardiomyocytes and uphold the balance of these ions to ensure proper cardiac function.

Accurately determining changes in ion concentrations poses a significant challenge within research. It is understood that alterations in ion concentrations manifest in variations in the action potential, with different types of changes leading to distinct action potential forms. As such, our objective is to forecast ion concentration changes by analyzing the shape of the action potential. The impact of diverse ion concentration modifications on the action potential in cardiomyocytes has been extensively explored. For example, an increase in extracellular potassium ion concentration raises the resting membrane potential, shortens the action potential duration (APD), and diminishes membrane excitability [7,8]. A rise in extracellular potassium ion concentration to 10 mmol/L can mitigate APD alternans [9]. Conversely, elevating extracellular sodium ion concentration intensifies depolarization and prolongs the APD [10]. Luo and Rudy utilized mathematical models to anticipate changes in the action potential based on alterations in intracellular calcium ion concentration [11]. However, research distinguishing between changes in ion concentrations inside and outside the cardiomyocyte membrane based solely on the shape of the action potential has not yet been conducted. This is the first research objective of the present study.

Previous studies have shown that changes in extracellular potassium ion concentration primarily affect the resting potential and APD of cardiomyocytes, thereby influencing their excitability [7,8]. In myocardial tissue, such alterations can impact wave propagation. This prompts us to investigate whether variations in potassium ion concentration can induce the spontaneous generation of spiral waves in myocardial tissue. This is the second research objective of the present study. In the heart, cardiomyocytes comprise only a small proportion of the cells, with the majority being non-cardiomyocytes, among which fibroblasts are the most numerous [12,13]. As the heart ages, it undergoes remodeling, with fibroblasts proliferating and differentiating into myofibroblasts [14,15]. It has been extensively demonstrated that there is mutual coupling between cardiomyocytes and fibroblasts (including myofibroblasts), known as myocyte-fibroblast coupling (M-F coupling) [16–18]. This means that fibroblasts in myocardial tissue can influence the electrophysiological properties of cardiomyocytes [19,20]. Qu et al. discovered that when the extracellular potassium ion concentration is low, cardiomyocytes exhibit early afterdepolarizations (EADs) [3]. Furthermore, when cardiomyocytes are coupled with fibroblasts, a decrease in extracellular potassium ion concentration exacerbates the formation of EADs, highlighting the significant impact of fibroblasts on cardiomyocytes [21]. Therefore, our study considers myocardial tissue to include both fibroblasts and cardiomyocytes.

For the first research objective, we employed machine learning methods. Machine learning algorithms are capable of efficiently processing large datasets to uncover hidden patterns and relationships. These advantages have led to their widespread application across various fields. In medical diagnostics, machine learning algorithms have been effectively combined with theoretical and experimental methods, yielding significant results [22–24]. Redkar et al. employed wrapper feature selection and class balancing techniques to predict drug–target interactions. They evaluated the effectiveness of different machine learning algorithms, such as Decision Tree, Extreme Gradient Boosting, Gaussian Naive Bayes, K-Nearest Neighbor, and Random Forest [25]. Lancaster et al. combined physiological modeling, statistical analysis, and machine learning to create a classifier that differentiates between proarrhythmic and non-proarrhythmic drugs, utilizing metrics from action potentials and intracellular calcium waveforms [26]. Ahme et al. successfully implemented a one-dimensional Convolutional Neural Network (1D-CNN) model for arrhythmia classification, achieving an accuracy of 99% on the test set [27]. In the investigation of cardiac electrophysiological mechanisms, the integration of machine learning algorithms has proven to be particularly significant [28,29]. The fusion of electrophysiological models with machine learning techniques has emerged as a powerful and effective

research approach [30–32]. Abnormal propagation of electrical waves in the heart can lead to the formation of spiral waves, triggering ventricular tachycardia (VT). These spiral waves breaking up can result in ventricular fibrillation (VF), a condition that can quickly become life-threatening. Mulimano et al. successfully identified patterns of unbroken and broken spiral waves through the use of CNN, offering a valuable tool for spiral wave identification [33]. In a separate study, Jeong et al. utilized an Artificial Neural Network (ANN) model to predict changes in ion channel conductance by comparing abnormal action potentials with standard action potentials. This model demonstrated an accuracy rate of 98% [34].

To predict ion concentration changes based on variations in action potentials, we developed a machine learning model using the ANN. The dataset was acquired through electrophysiological simulations using the Ten Tusscher-Noble-Noble-Panfilov (TNNP) human ventricular model of a single cardiomyocyte [35]. Sodium, potassium, and calcium ion concentrations inside and outside the cardiomyocyte membrane were systematically adjusted, and the subsequent action potentials were recorded. A total of 850 unique action potential variation curves were generated and utilized for training the ANN model. The findings demonstrated that the model successfully predicted ion concentration fluctuations from the action potential data with a high accuracy of 98.8% on the test set.

For the second research task, to more accurately reflect the complexity of the human heart, we constructed a composite myocardial tissue model that included both cardiomyocytes and fibroblasts. The primary component of the composite myocardial tissue was a two-dimensional layer of myocardial tissue, with certain regions locally covered by a specific density of fibroblasts. We explored the impact of K_0 variations on wave propagation in composite myocardial tissue with M-F coupling. We found that changes in K_0 within the composite myocardial tissue can either trigger or suppress cardiomyocyte excitation. Under specific structural configurations within the composite tissue, appropriate adjustments to K_0 can lead to the spontaneous generation of single spiral waves, symmetric spiral wave pairs, and asymmetric double spiral waves. Real heart tissue is complex and influenced by factors such as disease or fibrosis, leading to the spontaneous occurrence of spiral waves. Since K_0 can change due to diseases, the phenomena observed in this study are likely to occur in real hearts. This study is the first to demonstrate that changes in extracellular potassium ion concentration can spontaneously generate spiral waves in composite myocardial tissue.

The main contributions of this article are summarized as follows:

1. We established a dataset of myocardial cell action potentials corresponding to changes in the concentrations of various ion currents inside and outside the cell membrane. Based on this dataset, we developed a new ANN classification model that can accurately predict ion current concentration changes from action potential variations. The accuracy of the model in the test set is 0.988.
2. We have discovered a mechanism for the spontaneous generation of spiral waves in the heart. When certain specific structures are present within composite myocardial tissue, changes in the extracellular potassium ion concentration can trigger the spontaneous generation of spiral waves by myocardial cells in the composite tissue.

The rest of the paper is organized as follows: Section 2 describes the models and methods used for the two objectives. Section 3 presents the results of the two objectives. Section 4 discusses the results of each objective separately. Section 5 concludes the study and outlines future research directions.

2. Materials and Methods

2.1. Constructing the ANN Classification Model: Predicting Ion Concentration Changes Based on Action Potential Curves

2.1.1. Electrophysiological Cell Model

Cardiac cells are composed of cytoplasm and various ions that can move and create currents, resulting in changes in the membrane potential of cardiomyocytes. In the absence

of external stimuli, a cardiomyocyte remains in a resting state, characterized by a stable membrane potential difference across the cell membrane, known as the resting potential. This resting potential is primarily maintained by the outward flow of potassium ions. The formation of action potentials in cardiomyocytes is closely related to ion currents across the cell membrane. Since this study focuses on ventricular cardiomyocytes, we will use them as an example to describe the process of action potential formation. The action potential in ventricular cardiomyocytes includes the phases of depolarization and repolarization. The depolarization phase, also known as phase 0, occurs when external stimuli cause the membrane potential to reach the threshold. This triggers the opening of sodium channels in the cell membrane, leading to a rapid influx of sodium ions and a swift rise in the membrane potential. By the end of phase 0, calcium ions also begin to flow into the cell, while the outward flow of potassium ions temporarily decreases. The repolarization phase consists of four stages: phase 1, phase 2, phase 3, and phase 4, during which the cardiomyocyte gradually returns to its resting state. Phase 1, also known as the initial rapid repolarization phase, is characterized by the cessation of sodium ion influx and a transient outward flow of potassium ions. Phase 2, or the plateau phase, involves a slow influx of calcium ions and continued outward flow of potassium ions, with the cardiomyocyte in a refractory period, making it less responsive to external stimuli. Phase 3 is the terminal rapid repolarization phase, where calcium ion influx stops and potassium ions flow out rapidly. Phase 4, known as the resting phase, involves the sodium-potassium pump and sodium-calcium exchange mechanisms restoring ion concentrations inside and outside the cell membrane to pre-stimulus levels.

To obtain more accurate data on the variation of action potentials with ion concentration, this study utilizes data from the human heart model proposed by Ten Tusscher et al. in 2004, commonly referred to in the literature as the Ten Tusscher-Noble-Noble-Panfilov (TNNP) human heart model [35]. The experimental data used in this model encompass the major ion currents, comprehensively reflecting the changes in ion concentration through the changes in currents. Therefore, we employed the single-cell TNNP model for electrophysiological simulations. The dynamical equations of the model are as follows:

$$\frac{dV}{dt} = -\frac{I_{ion} + I_{stim}}{C_m}, \tag{1}$$

$$I_{ion} = I_{Na} + I_{K1} + I_{to} + I_{Kr} + I_{Ks} + I_{CaL} + I_{NaCa} + I_{NaK} + I_{pCa} + I_{pK} + I_{bCa} + I_{bNa}. \tag{2}$$

where V is the myocardial cell membrane voltage (in mV), t is the time (in ms), $C_m = 1.0$ μF/cm^2 is the membrane capacitance of the cardiomyocyte, I_{ion} is the sum of all transmembrane ionic currents, and I_{stim} is the externally applied stimulus current. The meanings and expressions of each ion current are shown in Table 1. In Table 1, E_{Na}, E_K, E_{Ks}, and E_{Ca} represent the reversal potentials of their respective ion currents, respectively. Their expressions are as follows:

$$E_X = \frac{RT}{zF}\log\frac{X_0}{X_i} \text{for } X = Na^+, K^+, Ca^{2+}, \tag{3}$$

$$E_X = \frac{RT}{F}\log\frac{K_0 + p_{KNa}Na_0}{K_i + p_{KNa}Na_i}. \tag{4}$$

where Na_0 and Na_i represent the extracellular and intracellular concentrations of sodium ions, respectively; K_0 and K_i represent the extracellular and intracellular concentrations of potassium ions, respectively; Ca_0 and Ca_i represent the extracellular and intracellular concentrations of calcium ions, respectively. Under normal conditions, $Na_0 = 140$ mM, $Na_i = 11.6$ mM, $K_0 = 5.4$ mM, $K_i = 138.3$ mM, $Ca_0 = 2.0$ mM, $Ca_i = 0.00002$ mM. Unless otherwise specified, other variables in the model represent the same meanings and values as in reference [35].

Table 1. Meaning and expression for each ionic current in the TNNP model.

Ion Current Expression	Ion Current Meaning
$I_{Na} = G_{Na} m^3 hj(V - E_{Na})$	Fast Na^+ Current
$I_{CaL} = G_{CaL} dff_{Ca} 4 \frac{VF^2}{RT} \frac{Ca_i e^{2VF/RT} - 0.341 Ca_0}{e^{2VF/RT} - 1}$	L−type Ca^{2+} Current
$I_{to} = G_{to} rs(V - E_K)$	Transient Outward Current
$I_{Ks} = G_{Ks} {x_s}^2 (V - E_{Ks})$	Slow Delayed Rectifier Current
$I_{Kr} = G_{Kr} \sqrt{\frac{K_0}{5.4}} x_{r1} x_{r2} (V - E_K)$	Rapid Delayed Rectifier Current
$I_{K1} = G_{K1} \sqrt{\frac{K_0}{5.4}} x_{K1\infty} (V - E_K)$	Inward Rectifier K^+ Current
$I_{NaCa} = k_{NaCa} \frac{e^{\gamma VF/RT} Na_i^3 Ca_0 - e^{(\gamma-1)VF/RT} Na_0^3 Ca_i \alpha}{(K_{mNai}^3 + Na_0^3)(K_{mCa} + Ca_0)(1 + k_{sat} e^{(\gamma-1)VF/RT})}$	Na^+/Ca^{2+} Exchanger Current
$I_{NaK} = P_{NaK} \frac{K_0 Na_i}{(K_0 + K_{mK})(Na_i + K_{mNa})(1 + 0.1245 e^{-0.1VF/RT} + 0.0353 e^{-VF/RT})}$	Na^+/K^+ Pump Current
$I_{pCa} = G_{pCa} \frac{Ca_i}{K_{pCa} + Ca_i}$	Plateau Ca^{2+} Current
$I_{pK} = G_{pK} \frac{V - E_K}{1 + e^{(25-V)/5.98}}$	Plateau K^+ Current
$I_{bNa} = G_{bNa}(V - E_{Na})$	Background Ca^{2+} Current
$I_{bCa} = G_{bCa}(V - E_{Ca})$	Background K^+ Current

2.1.2. Dataset Description

To obtain the dataset of the action potentials corresponding to changes in various ion concentrations, we set six variables: Na_0, Na_i, K_0, K_i, Ca_0, and Ca_i. We introduced μ to adjust the ion concentrations. Based on the typical range of ion concentration variations, the value of μ ranges from $[0.3, 0.99] \cup [1.01, 2.0]$, with an increment of 0.01. Thus, the ion concentrations were varied as $\mu \cdot Na_0$, $\mu \cdot Na_i$, $\mu \cdot K_0$, $\mu \cdot K_i$, $\mu \cdot Ca_0$, and $\mu \cdot Ca_i$, resulting in 170 values for each variable. We sequentially varied the six variables to obtain action potential data under different ion concentrations, with a basic cycle length of 600 ms, as shown by the black action potential curves in Figure 1. The red curve in Figure 1 represents the action potential under normal conditions ($\mu = 1$).

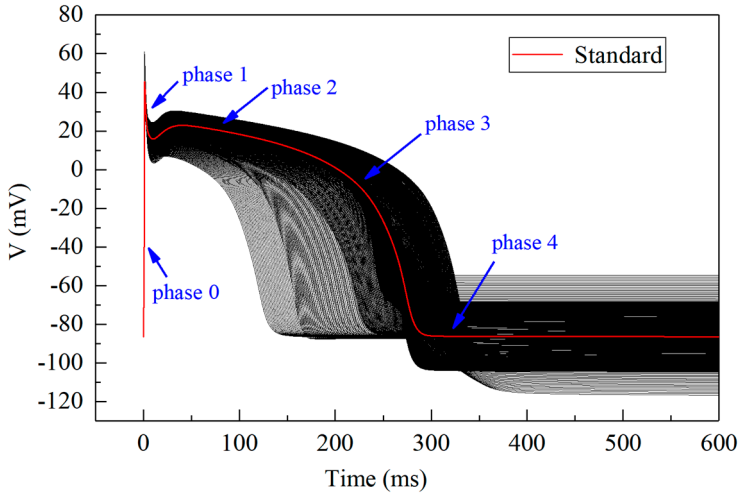


Figure 1. Action potential variation curves under different ion concentrations. The red curve represents the standard action potential variation curve under normal ion concentrations, while the blue arrows indicate the different phases of the standard action potential.

Figure 2 illustrates the changes in action potentials corresponding to variations in the concentrations of sodium, potassium, and calcium ions inside and outside the cell membrane. From Figure 2, it can be observed that changes in sodium ion concentrations primarily affect phases 0, 2, and 3 of the action potential, as shown in Figure 2a,b. This mainly manifests in the degree of depolarization of the cell membrane and APD. Potassium ion concentration changes mainly influence phases 0, 3, and 4 of the action potential, as

illustrated in Figure 2c,d, substantially impacting the degree of depolarization of the cell membrane, APD, and the resting potential of cardiomyocytes. Changes in extracellular calcium ion concentration primarily affect phases 1, 2, and 3 of the action potential, as seen in Figure 2e, mainly influencing the plateau phase and APD. In Figure 2f, the normal value of intracellular calcium ion concentration is 0.00002 mM. Within the range of μ values, changes in calcium ion concentration are minimal, and thus their effect on the action potential is negligible. Therefore, this study disregards the variable of intracellular calcium ion concentration.

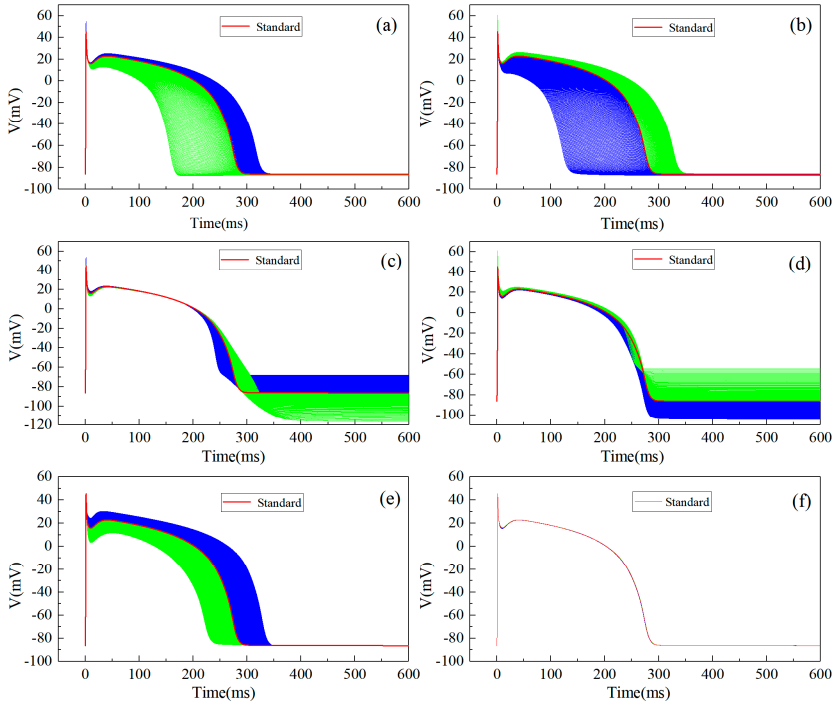


Figure 2. Action potentials corresponding to variations in the concentrations of sodium, potassium, and calcium ions inside and outside the cell membrane. The red curve represents the standard action potential curve under normal ion concentrations, the blue curve represents the action potential changes with increased ion concentrations, and the green curve represents the action potential changes with decreased ion concentrations. (**a**) Na_0; (**b**) Na_i; (**c**) K_0; (**d**) K_i; (**e**) Ca_0; (**f**) Ca_i.

Based on the above, our dataset comprises five variables: Na_0, Na_i, K_0, K_i, and Ca_0, categorized into five classes. Each class contains action potential data with 170 values, corresponding to 170 different action potentials. Therefore, the dataset contains a total of 850 samples. During numerical simulations, we recorded the voltage value every 0.02 ms, resulting in 30,000 voltage values for each sample.

2.1.3. Dataset Prepossessing

Before modeling, we processed the dataset as follows:

1. For each sample, we selected a voltage value at 0.4 ms intervals, resulting in 1500 voltage values per sample;
2. The dataset was standardized to improve the model's stability and performance;
3. The dataset was randomly split into training and testing sets, with 850 samples divided into training and testing datasets in an 8:2 ratio.

2.1.4. ANN Model Construction

To predict ion concentrations, we constructed an ANN model with three fully connected layers. The first input layer consisted of 64 neurons, the second hidden layer contained 32 neurons, and the final output layer included 5 neurons, corresponding to the

five types: Na_0, Na_i, K_0, K_i and Ca_0. We selected the ReLU activation function because it provides nonlinear fitting capabilities without causing the vanishing gradient problem. For the final layer, we chose the softmax activation function to convert the output into a probability distribution across the categories.

The model was trained using the Adam optimizer with its default hyperparameters and the cross-entropy loss function, with accuracy on the validation set monitored throughout the training process. Twenty percent of the training data was allocated as the validation set. The training process was set for 200 epochs with a batch size of 50. To mitigate the risk of overfitting caused by the limited data, we assessed the model's performance through five-fold cross-validation. After training, we evaluated the model's performance, with the results detailed in Section 3. The workflow of the entire method is shown in Figure 3.

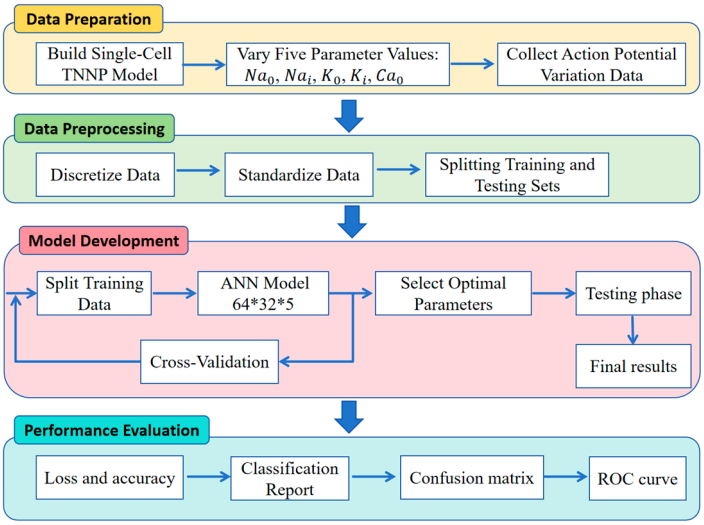


Figure 3. The workflow of ion concentration prediction.

2.2. Constructing the Mathematical Model of Composite Myocardial Tissue: Exploring the Spontaneous Generation of Spiral Waves

Abnormal ion concentrations in cardiomyocytes can result in abnormal action potential curves, as illustrated in Figure 1, increasing the likelihood of spiral waves forming in myocardial tissue. The presence of spiral waves in myocardial tissue is a concerning indicator, as their presence frequently results in arrhythmias [36]. Figure 2 illustrates the varying impacts of different ion concentrations inside and outside the cardiomyocyte membrane on action potentials. For instance, as depicted in Figure 2c, changes in K_0 primarily influence APD and resting potential. Decreasing K_0 lengthens APD and the effective refractory period of the cardiomyocyte, while also reducing the resting potential, resulting in hyperpolarization. Conversely, increasing K_0 shortens the APD and increases the resting potential, leading to depolarization. These alterations influence the excitability of the medium and alter the propagation of electrical signals within myocardial tissue. This study utilizes a composite myocardial tissue comprising both cardiomyocytes and fibroblasts to explore how changes in K_0 can induce the spontaneous formation of spiral waves within the tissue.

The Luo-Rudy Phase I (L-R Phase I) heart model, which includes only the five major currents in the heart, is considered relatively simple yet accurately describes the dynamic behavior of cardiomyocytes [37]. Due to its simplicity and accuracy, this model is widely utilized in research. For our simulations on a two-dimensional myocardial tissue, taking into account computational cost, we incorporated the L-R Phase I heart model along with a passive fibroblast model [38]. The main component of the composite myocardial tissue is a two-dimensional layer of myocardial tissue measuring 8.4 cm $\times$ 8.4 cm, discretized into a grid of 300 $\times$ 300 points. The coordinates of the grid points are denoted as (i, j), with integer values ranging from 1 to 300. Myocardial tissue is partially covered with a

certain density of fibroblasts, which couple with cardiomyocytes through gap junctions in the covered area. Since fibroblasts are much smaller than cardiomyocytes, it can be assumed that each grid point can accommodate only one cardiomyocyte but can hold n fibroblasts. Therefore, one cardiomyocyte is electrically coupled with n fibroblasts, with n referred to as the cell coupling number. Because fibroblasts are overlaying cardiomyocytes, wave propagation mainly relies on the cardiomyocytes, so the electrical coupling between fibroblasts is ignored in this study. In the model, the values of some parameters are set as follows: the coupling strength of M-F coupling $G_{gap} = 4$ nS, the resting membrane potential of fibroblasts $E_f = -45$ mV, and the membrane conductivity of fibroblasts $G_f = 4$ nS. In the L-R Phase I cardiac model, the normal concentration of extracellular potassium ions is 5.4 mmol/L. We set the concentration of extracellular potassium ions as a variable. The detailed mathematical model of the composite myocardial tissue is provided in Appendix A.

In numerical simulation, no-flux boundary conditions are used in all simulations. The time derivative is obtained using the first order Euler forward difference method and the second order spatial derivative is obtained using the central difference method with fixed time step of $\Delta t = 0.02$ ms and spatial step of $\Delta x = \Delta y = 0.028$ cm. The initial state of the composite medium is set as follows: all cells are in a resting state, with the initial membrane potentials of cardiomyocytes and fibroblasts set to $V_m = -84$ mV, and $V_f = -55$ mV.

3. Results

3.1. Performance Evaluation of the ANN Classification Model

This study utilized several metrics to evaluate the model's performance in predicting ion concentration changes. Details on performance metrics are provided in Appendix B. Through five-fold cross-validation, we observed an average accuracy of 0.98 on the test sets, indicating that the model does not exhibit severe overfitting. Among all the folds, we selected the results from the fold that demonstrated the best performance. The accuracy and loss curves of the model are illustrated in Figure 4. As seen in Figure 4, both the training and validation curves gradually stabilize with the increase in training epochs. The trained model achieved an accuracy of 0.993 on the training set and 0.988 on the test set.

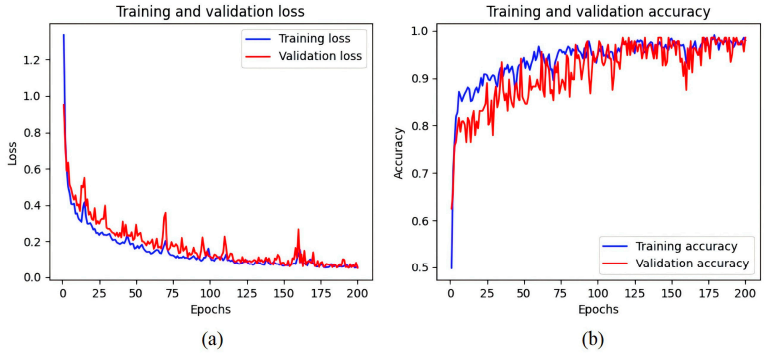


Figure 4. Accuracy and loss curves of the ANN model. (**a**) Accuracy Curve; (**b**) Loss Curve.

Additionally, we evaluated the model's precision, recall, F1-score, and support on both the training and test datasets. As shown in Table 2, the changes in K_0, K_i, and Ca_0 were accurately classified in the training dataset, with all achieving precision, recall, and F1-score values of 1.0. The model's performance on the test dataset reflected its generalization ability. The data in Table 2 indicate that the model achieved an average precision of 0.989, an average recall of 0.988, and an average F1-score of 0.988 on the test set, demonstrating the model's strong generalization capability.

Table 2. Classification report of the ANN model.

Matrix	Training Dataset						Testing Dataset					
	Na_0	Na_i	K_0	K_i	Ca_0	Average	Na_0	Na_i	K_0	K_i	Ca_0	Average
precision	0.99	0.98	1.00	1.00	1.00	0.993	0.97	1.00	1.00	1.00	0.97	0.989
recall	0.98	0.99	1.00	1.00	1.00	0.993	1.00	0.94	1.00	1.00	1.00	0.989
F1-score	0.98	0.98	1.00	1.00	1.00	0.993	0.98	0.97	1.00	1.00	0.99	0.988
support	139	136	136	135	134	-	31	34	34	35	36	-

Figures 5 and 6 illustrate the confusion matrices and ROC curves of the model on the training and test sets, respectively. As shown in Figure 5a, the training set predictions for K_0, K_i, and Ca_0 were accurate. Among the 139 samples where changes in Na_0 led to action potential variations, 3 were misclassified as changes in Na_i, with an error rate of only 0.02. For the 136 samples where changes in Na_i led to AP variations, 2 were misclassified as changes in Na_0, with an error rate of only 0.01. In the test set, as shown in Figure 5b, only 2 samples in the Na_i category were misclassified, while the other four categories were accurately predicted.

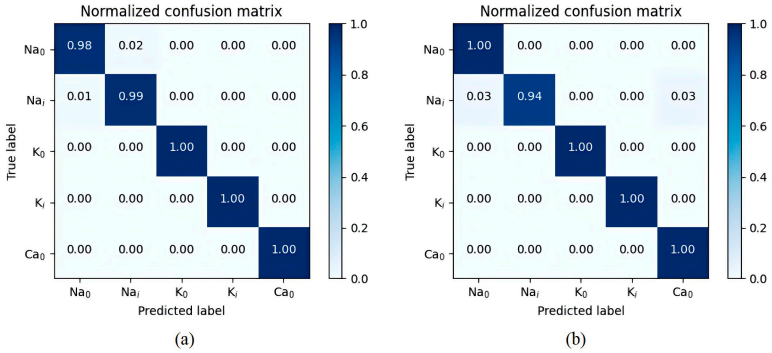


Figure 5. Confusion matrix of the ANN model. (**a**) Training-based confusion matrix; (**b**) test-based confusion matrix.

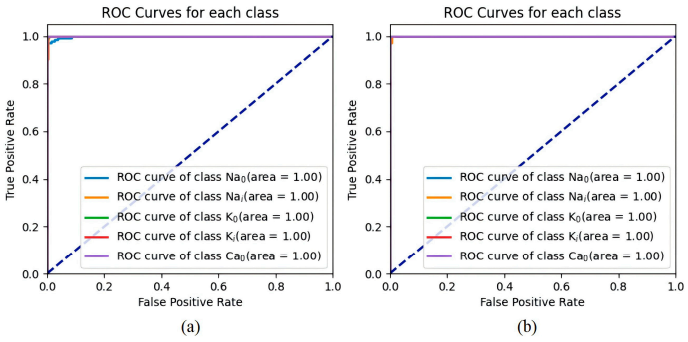


Figure 6. ROC curve of the ANN model. (**a**) Training-based ROC curve; (**b**) test-based ROC curve.

In the ROC curve, the $y = x$ line represents a random classification curve. All five classified ROC curves of the ion concentration were distributed in the left area of the random classification curve, and all area under the curve (AUC) values were 1, implying that all of the ion channel conductance were accurately classified. Figure 6 shows a perfect score in all classes in the training and testing datasets.

3.2. Three Structures of the Composite Cardiac Tissue and the Spontaneous Generation of Spiral Waves

In this section, we introduce the three structures of the composite cardiac tissue and the mechanisms of spiral wave generation. To clearly illustrate the formation process of

spiral waves, we plotted the pattern of the membrane potential in the cardiac tissue. The brightness in the pattern indicates the voltage levels of the cardiac cells.

3.2.1. The First Configuration of Composite Cardiac Tissue and the Generation of a Single Spiral Wave

In the composite cardiac tissue, fibroblasts are uniformly distributed in two regions, Region 1 and Region 2. The spatial coordinates (i, j) for Region 1 are $i \in [100, 129]$, $j \in [1, 50]$, and for Region 2 are $i \in [130, 160]$, $j \in [1, 200]$. The extracellular potassium ion concentration in Region 1 is denoted as $K_{0,1}$, and in Region 2 as $K_{0,2}$. The extracellular potassium ion concentrations in these two regions vary over time as follows:

$$K_{0,1} = 3.5\text{mmol/L},\ K_{0,2} = 10.0\text{mmol/L}\ if\ \ t < 130\ \text{ms} \tag{5}$$

$$K_{0,1} = 10.0\text{mmol/L},\ K_{0,2} = 2.5\text{mmol/L}\ if\ \ 130\ \text{ms} \leq t < 210\ \text{ms} \tag{6}$$

$$K_{0,1} = 5.4\text{mmol/L},\ K_{0,2} = 5.4\text{mmol/L}\ if\ t \geq 210\ \text{ms} \tag{7}$$

Numerical simulation results indicate that when K_0 varies according to Equations (5)–(7), a single spiral wave can a single spiral wave can be spontaneously generated in the composite cardiac tissue. The formation process of the spiral wave is illustrated in Figure 7. Initially, since $K_{0,1}$ in Region 1 is below the normal extracellular potassium concentration of 5.4 mmol/L, the myocardial cells in Region 1 are excited first at $t = 35$ ms, as shown in Figure 7b. This gradually forms a target wave in the system, with the myocardial cells in Region 2 being sequentially excited from the bottom to the top during this process. Next, at $t = 180$ ms, as shown in Figure 7e, the target wave is about to move out of the system boundary. At this time, since $K_{0,1}$ in Region 1 is higher than the normal extracellular potassium concentration, and $K_{0,2}$ in Region 2 is lower than the normal concentration, the myocardial cells at the lower end of Region 2 have already spontaneously excited, generating a target wave that propagates outward. However, the target wave cannot propagate in other parts of Regions 1 and 2 because the myocardial cells are still in the effective refractory period. The myocardial cells on the right side of Region 2 have exited the refractory period, so the target wave gradually propagates to the right, appearing as a quarter-circular wave. The target wave then excites the myocardial cells on the right side of Region 2 upward, as shown in Figure 7f. Finally, at $t = 270$ ms, as shown in Figure 7g, the extracellular potassium ion concentrations in Regions 1 and 2 have returned to normal values, causing the myocardial cells at the top of Region 2 to return to the resting state. The target wave just reaches this area, allowing it to propagate into Region 2, forming the wave tip, which then gradually evolves into a single spiral wave.

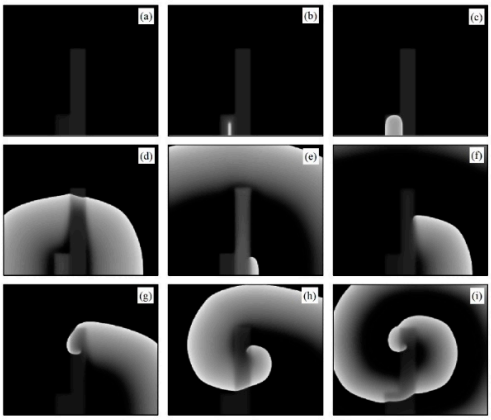


Figure 7. The pattern of the membrane potential at different time moments. (**a**) $t = 10$ ms; (**b**) $t = 35$ ms; (**c**) $t = 40$ ms; (**d**) $t = 110$ ms; (**e**) $t = 180$ ms; (**f**) $t = 230$ ms; (**g**) $t = 270$ ms; (**h**) $t = 315$ ms; (**i**) $t = 2805$ ms.

3.2.2. The Second Composite Cardiac Tissue Configuration and the Generation Process of Spiral Wave Pairs

In this configuration of the composite cardiac tissue, the middle region of the myocardial layer, with spatial grid coordinates $i, j \in [80, 220]$, is uniformly covered with fibroblasts. The extracellular potassium ion concentration in this region varies over time as follows:

$$K_0 = 3.5\text{mmol/L}\ if\ \ t < 250\ \text{ms} \tag{8}$$

$$K_0 = 5.4\text{mmol/L}\ if\ \ t \geq 250\ \text{ms} \tag{9}$$

Numerical simulation results indicate that when K_0 varies according to Equations (8)–(9), spiral wave pairs can be spontaneously generated in the composite cardiac tissue. The formation process of the spiral wave pairs is illustrated in Figure 8. Initially, at $t = 40$ ms, due to K_0 in the fibroblast-covered region being lower than the normal concentration, myocardial cells in the covered region self-excite and generate a target wave that propagates outward, as shown in Figure 8b. However, after excitation, these myocardial cells cannot return to the resting state and remain in the effective refractory period, as seen in Figure 8d, thus turning the fibroblast-covered area into a wave-blocking zone. Subsequently, at $t = 168$ ms, a plane wave with a width of 10 grid points is introduced at the lower boundary of the system to simulate the plane wave generated by the sinoatrial node. When this plane wave encounters the covered region, as illustrated in Figure 8e, it is blocked and broken at the boundary of the covered region and can only propagate along the boundary. Then, at $t = 305$ ms, as shown in Figure 8f, the plane wave is about to cross the covered region, where K_0 has returned to the normal concentration, allowing the myocardial cells to return to the resting state. The previously blocked area becomes passable again, and the broken plane wave propagates into the covered region, forming two spiral wave heads. Finally, the collision of the two spiral waves formed a symmetrical spiral wave pair.

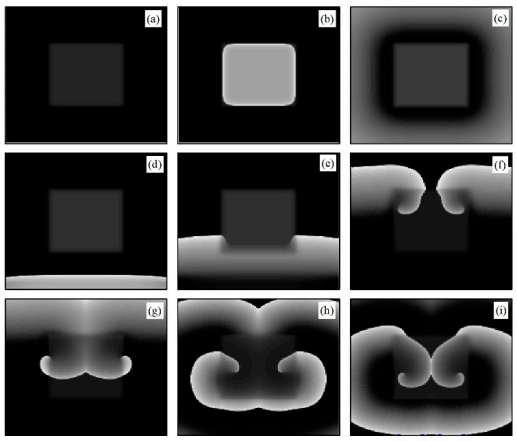


Figure 8. The pattern of the membrane potential at different time moments. (**a**) $t = 20$ ms; (**b**) $t = 40$ ms; (**c**) $t = 120$ ms; (**d**) $t = 180$ ms; (**e**) $t = 225$ ms; (**f**) $t = 305$ ms; (**g**) $t = 330$ ms; (**h**) $t = 5740$ ms; (**i**) $t = 5840$ ms.

3.2.3. The Third Composite Myocardial Tissue Configuration and the Formation Process of Double Spiral Wave

The uniform distribution of fibroblasts is a special case; in most scenarios, fibroblasts are distributed non-uniformly. In this section, we discuss the spontaneous generation of spiral waves under a gradient distribution of fibroblast density. In the composite myocardial tissue, fibroblasts are randomly distributed within the region $i \in [81, 220]$, $j \in [51, 250]$, with the fibroblast density (the ratio of occupied grid points to total grid points) varying as a gradient: higher density on the left, lower density on the right. Specifically, the region $i \in [81, 220]$ is divided into seven sub-regions: Region 1, $i \in [81, 100]$, fibroblast density is 100%; Region 2, $i \in [101, 120]$, fibroblast density is 90%; Region 3, $i \in [121, 140]$, fibroblast

density is 80%; Region 4, $i \in [141, 160]$, fibroblast density is 70%; Region 5, $i \in [161, 180]$, fibroblast density is 60%; Region 6, $i \in [181, 200]$, fibroblast density is 50%; and Region 7, $i \in [201, 220]$, fibroblast density is 40%. The potassium ion concentration in these seven regions changes synchronously over time, following the pattern described below:

$$K_0 = 3.5\text{mmol/L}\ if\ \ t < 40\ \text{ms} \tag{10}$$

$$K_0 = 8.0\text{mmol/L}\ \ if\ \ 40\ \text{ms} \leq t < 120\ \text{ms} \tag{11}$$

$$K_0 = 3.0\text{mmol/L}\ \ if\ \ 120\ \text{ms} \leq t < 160\ \text{ms} \tag{12}$$

$$K_0 = 5.4\text{mmol/L}\ if\ \ t \geq 160\ \text{ms} \tag{13}$$

Numerical simulation results indicate that when K_0 varies according to Equations (10)–(13), a double spiral wave can be spontaneously generated in the composite cardiac tissue. The formation process of double spiral waves is illustrated in Figure 9. Initially, when K_0 in the covered region is lower than the normal extracellular potassium concentration, regions with higher fibroblast density will self-excite first, generating target waves that propagate outward, as shown in Figure 9b. Subsequently, when K_0 in the covered region is higher than the normal extracellular potassium concentration, the myocardial cells return to a resting state. However, due to the varying fibroblast densities in the covered region, the time it takes for the myocardial cells to return to the resting state differs across regions. Then, during the period 120 ms $\leq t <$ 160 ms, K_0 in the covered region again falls below the normal extracellular potassium concentration, causing myocardial cells in areas with higher fibroblast density to excite once more, as depicted in Figure 9d. Myocardial cells that are in the refractory state become wave-blocking zones, so the wave does not spread outward widely; instead, a few myocardial cells that have returned to the resting state are re-excited, as shown in Figure 9e. The excitation wave propagates along the edge of the blocking zone. Finally, when K_0 in the covered region returns to normal, the myocardial cells within the blocking zones quickly return to the resting state. The excitation wave then starts to propagate inward, forming two wave tips, as shown in Figure 9f. These further evolve into a pair of spiral waves, as illustrated in Figure 9g. As time progresses, the distance between the two wave tips increases, resulting in the formation of a double spiral wave. Due to the uneven distribution of fibroblasts, the double spiral wave was not perfectly symmetrical.

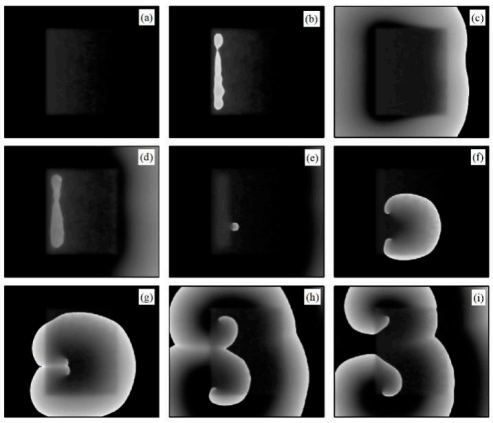


Figure 9. The pattern of the membrane potential at different time moments. (**a**) t = 20 ms; (**b**) t = 40 ms; (**c**) t = 115 ms; (**d**) t = 165 ms; (**e**) t = 190 ms; (**f**) t = 230 ms; (**g**) t = 255 ms; (**h**) t = 1125 ms; (**i**) t = 7040 ms.

4. Discussion

In this study, we performed electrophysiological simulations of myocardial cells to accomplish the following two tasks:

1. We predicted and classified the changes in ion concentration based on action potential shapes using a machine learning algorithm with ANN layers. Through electrophysiological simulations of single myocardial cells, we generated a dataset of action potentials corresponding to changes in five ion concentrations. We developed an ANN classification model that accurately predicts ion concentration changes based on action potential variations, achieving an accuracy of 0.988 on the test set.
2. We conducted electrophysiological simulations of a two-dimensional composite myocardial tissue. By structuring the tissue and altering the extracellular potassium ion concentration K_0, we induced self-excitation in myocardial cells, resulting in the generation of single spiral wave, spiral wave pair, and double spiral wave within the two-dimensional composite myocardial tissue.

4.1. ANN Classification Model

This study presents an ANN model designed to predict ion concentration changes based on action potential variation curves. We focused on changes in five types of ion concentrations: Na_0, Na_i, K_0, K_i, and Ca_0. Using the TNNP single-cell electrophysiological model, we generated an AP dataset comprising 850 distinct AP variation curves, with each class including 170 action potential variation curves. The model achieved an accuracy of 0.988 under the current parameters, and other evaluation metrics also performed well, demonstrating that ion concentration changes can be accurately predicted based on action potential variation curves. Monitoring ion concentration changes in myocardial cells is challenging, yet normal ion concentration variations are crucial for maintaining a regular heart rate. Therefore, the model proposed in this study provides an effective method for predicting intracellular and extracellular ion concentration changes from action potential variation curves.

Additionally, we tested the ANN model with varying hidden layers, from one to three layers, and found that increasing the number of hidden layers did not significantly improve the model's performance. In fact, adding more layers increased the model's complexity, reducing its generalization ability. We also tested the model's performance by changing the training-to-testing dataset ratio to $60:40$, $70:30$, $75:25$, and $80:20$ to examine the model's sensitivity to the training dataset size. The results indicated that the training-to-testing ratio had no significant impact on the model's performance.

4.2. Spontaneous Generation of Spiral Waves in Myocardial Tissue

This study constructs a two-dimensional composite myocardial tissue partially covered by fibroblasts at a certain density. Due to this coverage, there is coupling between the myocardial cells and the fibroblasts in the covered region. When K_0 in the covered region varies over time following a specific pattern, the composite myocardial tissue exhibits the spontaneous generation of a single spiral wave, spiral wave pair, and a double spiral wave.

Fibroblasts are unexcitable cells. Their resting membrane potential is more depolarized than that of myocytes, and their membrane resistance is higher. Although fibroblasts cannot generate action potentials themselves, due to their high membrane resistance, they can passively mimic the electrical activity of the coupled myocardial cells under certain parameters, producing action potential-like responses similar to those of myocardial cells [18,39]. Since the resting membrane potential of fibroblasts is higher than that of myocardial cells, fibroblasts can play dual roles when coupled with myocytes. When the resting potential of fibroblasts is significantly higher than that of myocardial cells, fibroblasts act as a source of stimulus current, enhancing the excitability of the coupled myocardial cells and inducing their excitation. Conversely, if fibroblasts cannot generate stimulus current and require stimulus from myocardial cells to follow the membrane potential changes, they act as current sinks, suppressing the excitability of the coupled myocardial cells [40,41].

To analyze the mechanism of spontaneous spiral wave generation in myocardial cells within three different composite medium structures, we fixed the resting potential

of fibroblasts to $E_f = -45$ mV. The myocardial cells and fibroblasts were allowed to evolve from their initial states, and the effects of K_0 variations on both cell types were observed. For this purpose, we plotted Figure 10 to demonstrate the action potentials of myocardial cells and fibroblasts under different values of K_0. Figure 10a shows the changes in action potentials when the potassium concentration decreases, while Figure 10b shows the changes when the potassium concentration increases. In both subfigures, the black curves represent the action potential changes of myocardial cells and fibroblasts when $K_0 = 5.4$ mmol/L, the normal extracellular potassium concentration. In Figure 10, we present the following two scenarios:

- The changes in the action potentials of myocardial cells without coupling to fibroblasts, indicated by the dashed lines.
- The changes in the action potentials of myocardial cells and fibroblasts when they are coupled, indicated by the solid lines.

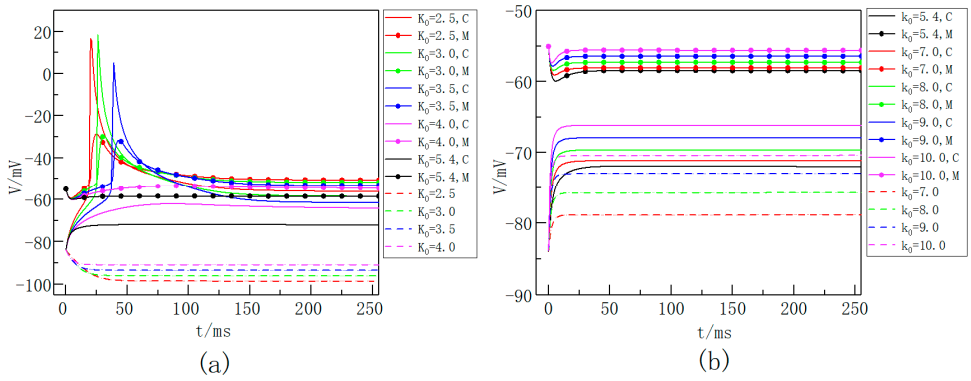


Figure 10. Changes in the action potentials of myocardial cells and fibroblasts for different K_0 values. The black curves in the figures represent the situation where the K_0 is at its normal value. The dashed lines show the changes in myocardial cell action potentials without coupling to fibroblasts. The solid lines indicate the action potential changes of myocardial cells (solid lines) and fibroblasts (dotted solid lines) when they are coupled. (**a**) The scenario with decreased K_0; (**b**) the scenario with increased K_0.

When cardiomyocytes are not coupled with fibroblasts, as shown by the dashed line in Figure 10a, lowering K_0 concentration results in a decreased membrane potential of the cardiomyocytes, indicating hyperpolarization. The lower the K_0 concentration, the greater the degree of cardiomyocyte hyperpolarization. This observation is consistent with the phenomenon observed in Figure 2c. When cardiomyocytes are coupled with fibroblasts, the solid line in Figure 10a reveals that at normal K_0 levels, the fibroblasts' higher resting potential causes depolarization in the coupled cardiomyocytes, as shown by the black solid line in Figure 10a. However, this depolarization is not sufficient to trigger spontaneous excitation; the cardiomyocytes remain in a mildly depolarized state. At $K_0 = 4.0$ mmol/L, the previously hyperpolarized cardiomyocytes, influenced by the fibroblasts, exhibit an increased degree of depolarization. When $K_0 = 3.5$ mmol/L, the hyperpolarization of the cardiomyocytes is more pronounced, resulting in an even lower membrane potential. In this case, the increased potential difference between the cardiomyocytes and fibroblasts enhances the current source effect of the fibroblasts, raising the membrane potential of the cardiomyocytes. When the membrane potential reaches the excitation threshold, spontaneous excitation occurs in the cardiomyocytes (as seen in the blue solid line in Figure 10a). Due to the influence of fibroblasts, the excited cardiomyocytes remain in a highly depolarized state, or the effective refractory period, and do not return to the resting state, making them unable to re-excite. As the K_0 decreases further, the hyperpolarization of the cardiomyocytes intensifies, resulting in an even lower membrane potential. The current source effect of the fibroblasts becomes stronger, leading to faster and greater spontaneous excitation in the cardiomyocytes, which then remain in the effective refractory period.

If K_0 increases, when cardiomyocytes are not coupled with fibroblasts, as indicated by the dashed line in Figure 10b, the elevation in K_0 leads to depolarization of the cardiomyocytes, resulting in an increase in their membrane potential. Moreover, the higher K_0, the greater the degree of depolarization in cardiomyocytes. This change is consistent with the observations in Figure 2c. When cardiomyocytes are coupled with fibroblasts, as shown by the solid line in Figure 10b, the influence of fibroblasts increases the degree of depolarization in cardiomyocytes. However, even with this increase, the membrane potential does not reach the excitation threshold, and thus the cardiomyocytes do not undergo excitation. Additionally, the membrane potentials of the cardiomyocytes are all less than -65 mV, indicating that the cardiomyocytes are in a relative refractory period. During this period, cardiomyocytes can respond to stimuli above the threshold by generating new excitations.

In summary, when K_0 decreases, cardiomyocytes undergo hyperpolarization. Coupling hyperpolarized cardiomyocytes with fibroblasts facilitates the spontaneous generation of action potentials, and the excited cardiomyocytes remain in the effective refractory period, preventing further excitation. Conversely, if K_0 increases, cardiomyocytes depolarize. When these depolarized cardiomyocytes are coupled with fibroblasts, the degree of depolarization increases, placing the cardiomyocytes in a relative refractory period, requiring stronger stimuli to excite the cells. These phenomena demonstrate that coupling cardiomyocytes with fibroblasts alters the excitability of cardiomyocytes in response to changes in K_0, either promoting or inhibiting excitation. This, in turn, makes it easier for spiral waves to form in myocardial tissue.

This study constructed three types of composite myocardial tissue structures and adjusted K_0 to simulate the spontaneous generation of spiral waves. Given the complexity of cardiac structure and its potential alterations due to disease or aging, myocardial tissue structures can change, and such changes are often unpredictable. Therefore, when designing the composite myocardial tissue structures, we considered scenarios with a single fibroblast-covered area, two fibroblast-covered areas, and areas with varying fibroblast densities. In each of these cases, we observed the spontaneous generation of spiral waves, indicating that dynamic changes in K_0 can induce spiral wave formation in complex cardiac environments through the self-excitation of cardiomyocytes.

5. Conclusions

This study presents a novel ANN classification model designed to predict ion concentration changes based on the action potential waveforms of cardiomyocytes. We developed a dataset comprising action potentials corresponding to varying ion concentrations and trained an ANN model using this dataset. Multiple performance evaluations of the model demonstrated high accuracy, stability, and robustness, showcasing its superior performance in predicting changes in cardiomyocyte ion concentrations. Given the difficulty in directly detecting ion concentration changes, our model offers a simple and efficient method with practical application value. Furthermore, this study reveals a mechanism for the spontaneous generation of spiral waves in the heart. It is found that in composite myocardial tissue containing both cardiomyocytes and fibroblasts, a decrease in K_0 leads to the spontaneous excitation of cardiomyocytes, which can readily induce the formation of spiral waves. To investigate this, we designed three structures of composite myocardial tissue and modulated K_0 in a specific manner, resulting in the generation of single spiral waves, spiral wave pairs, and double spiral waves in the tissue. During disease progression or cardiac aging, fibroblasts contribute to fibrosis and the formation of infarct scars, complicating the heart's structure, and K_0 can vary due to disease or medication. Therefore, our numerical simulation results might reflect real cardiac events, helping us understand how cardiac spiral waves spontaneously arise. However, due to the inherent complexity of cardiac structure, the myocardial tissue configurations we simulated are not exhaustive. In future research, we plan to explore a wider range of more realistic tissue structures, such as the impact of fibroblast infiltration into myocardial layers on wave propagation.

Currently, our machine learning model predicts ion concentrations. Since the gating variables of ion currents significantly impact ion flow, future research could involve developing machine learning models to predict the states of ion current gating variables.

Author Contributions: Conceptualization, J.B., Y.L. and L.W.; methodology, J.B. and A.T.; software, J.B.; validation, C.Z., Y.L., A.T., L.W., X.G. and Z.M.; formal analysis, J.B., C.Z., X.G. and Z.M.; investigation, Y.L., A.T. and L.W.; resources, Y.L., A.T. and L.W.; writing—original draft preparation, J.B., C.Z. and X.G.; writing—review and editing, J.B., C.Z., Y.L., A.T., L.W. and Z.M.; visualization, J.B.; supervision, Y.L., A.T. and L.W.; project administration, A.T.; funding acquisition, Y.L. and L.W. All authors have read and agreed to the published version of the manuscript.

Funding: This research was funded by the National Natural Science Foundation of China, grant number 62372494, the Guangdong Province College Youth Innovative Talent Project, grant number 2024KQNCX013, the Guangdong Engineering Centre Project, grant number 2024GCZX001, the Guangdong Province College Youth Innovative Talent Project, grant number 2023KQNCX132, and the Guangdong Key Disciplines Project, grant number 2021ZDJS138.

Data Availability Statement: The raw data supporting the conclusions of this article will be made available by the authors on request.

Conflicts of Interest: The authors declare no conflict of interest.

Appendix A

To investigate the spontaneous generation of spiral waves in the composite myocardial tissue due to variations in extracellular potassium ion concentration, we employed the L-R Phase I heart model and the passive fibroblast model. A composite myocardial tissue was constructed by partially covering a two-dimensional myocardial tissue layer with fibroblasts. The dynamical equations for the composite myocardial tissue are as follows:

$$\frac{\partial V_m}{\partial t} = -\frac{I_{ion}}{C_m} + \frac{n}{C_{mz}}\Omega\left(\vec{r}\right)G_{gap}\left(V_f - V_m\right) + D\nabla^2 V_m, \tag{A1}$$

$$I_{ion} = I_{Na} + I_{si} + I_K + I_{k1} + I_{kp} + I_b, \tag{A2}$$

$$\frac{\partial V_f}{\partial t} = -\frac{I_f}{C_f} + \frac{1}{C_f}\Omega\left(\vec{r}\right)G_{gap}\left(V_m - V_f\right), \tag{A3}$$

$$I_f = G_f\left(V_f - E_f\right). \tag{A4}$$

where V_m and V_f represent the membrane voltages of the cardiomyocytes and fibroblasts, respectively (in mV), $C_m = 1$ μF/cm^2 is the membrane capacitance of the cardiomyocytes, and the total membrane capacitances of the entire cardiomyocyte and fibroblast are $C_{mz} = 125$ pF and $C_f = 25$ pF, respectively [37], t is time (in ms), $D = 0.001$ cm^2/ms is the diffusion coefficient, I_{ion} is the total membrane currents of the cardiomyocytes (in μA/cm^2), and I_f is the total membrane currents of the fibroblasts (in nA). The meaning and expression for the ion currents of the cardiomyocytes are detailed in Table A1. n is the cell coupling number, $G_{gap} = 4$ nS is the coupling strength of the M-F coupling. $G_f = 4$ nS is the membrane conductance of the fibroblasts, and $E_f = -45$ mV is the resting potential of the fibroblasts. When the spatial point $\vec{r}$ is covered by fibroblasts, $\Omega\left(\vec{r}\right) = 1$; otherwise, $\Omega\left(\vec{r}\right) = 0$.

Table A1. Meaning and expression for each ionic current in the L-R model.

Ion Current Expression	Ion Current Meaning
$I_{Na} = \overline{G}_{Na} \cdot m^3 \cdot h \cdot j \cdot (V - E_{Na})$	the fast inward sodium ion current
$I_{Si} = \overline{G}_{Si} \cdot d \cdot f \cdot (V - E_{Si})$	the slow inward calcium ion current
$I_K = \overline{G}_K \cdot x \cdot x_i \cdot (V - E_K)$	the time-dependent potassium current
$I_{K1} = \overline{G}_{K1} \cdot K1_\infty \cdot (V - E_{K1})$	the time-independent potassium current
$I_{Kp} = \overline{G}_{Kp} \cdot K_p \cdot (V - E_{Kp})$	the plateau potassium current
$I_b = \overline{G}_b \cdot (V - E_b)$	the background leakage current

The variables m, h, j, d, f and x are the gating variables for the respective ion currents and satisfy the following type of differential equation:

$$\frac{dy}{dt} = \alpha_y(1.0 - y) - \beta_y y. \tag{A5}$$

where y represents the gating variables. In the aforementioned current and gating variable equations, $K1_\infty$, x_i, K_p, α_y, β_y are functions related to the membrane voltage, $\overline{G}$ represents the maximum conductance for each ion current, and E denotes the reversal potential of each ion current. Among these, $\overline{G}_{Na}$, $\overline{G}_{si}$, $\overline{G}_{kp}$, $\overline{G}_b$, and E_{Nb} are constants, while the maximum conductance and reversal potential of other ion currents depend on ion concentrations. The calculation expressions are as follows:

$$E_{Na} = \frac{RT}{F} \ln \frac{Na_0}{Na_i}, \tag{A6}$$

$$\overline{G}_K = 0.705 \sqrt{\frac{K_0}{5.4}}, \tag{A7}$$

$$E_K = \frac{RT}{F} \ln \frac{K_0 + PR_{NaK} \cdot Na_0}{K_i + PR_{NaK} \cdot Na_i}, \tag{A8}$$

$$\overline{G}_{K1} = 0.6047 \sqrt{\frac{K_0}{5.4}}, \tag{A9}$$

$$E_{K1} = \frac{RT}{F} \ln \frac{K_0}{K_i}, \tag{A10}$$

$$E_{Kp} = E_{K1}, \tag{A11}$$

$$E_{si} = 7.7 - 13.0287 \ln Ca_i. \tag{A12}$$

where $PR_{NaK} = 0.001883$ is the Na/K permeability ratio, $R = 8314$ J/kmolK is the universal gas constant, $F = 96485$ C/mol is the Faraday constant, $T = 310$ K is the temperature at which Luo and Rudy measured their data, $Na_i = 18$ mmol/L is the intracellular sodium ion concentration, $Na_0 = 140$ mmol/L is the extracellular sodium ion concentration, $K_i = 145$ mmol/L is the intracellular potassium ion concentration, $K_0 = 5.4$ mmol/L is the extracellular potassium ion concentration under normal conditions, and $Ca_0 = 1.8$ mmol/L is the extracellular calcium ion concentration. The intracellular calcium ion concentration evolves according to the following rule:

$$\frac{dCa_i}{dt} = -0.0001 I_{si} + 0.07(0.0001 - Ca_i). \tag{A13}$$

We used the extracellular potassium ion concentration K_0 as the control parameter, while other parameters were consistent with the literature [37]. From the above expressions, it is evident that variations in K_0 will affect $\overline{G}_K$, $\overline{G}_{K1}$, E_K and E_{K1}, subsequently influencing the corresponding ion currents. The changes in ion currents, in turn, affect the action potential.

Appendix B

The first study presented in this paper addresses a multi-class classification problem, therefore, we provide an overview of the relevant performance metrics here.

- Accuracy: Reflects the proportion of correctly predicted samples relative to the total sample size.

$$\text{Accuracy} = \frac{\text{Number of correctly predicted samples}}{\text{Total number of samples}} \tag{A14}$$

High accuracy indicates that the model can correctly predict the majority of samples' classes, while low accuracy suggests poor model performance.

- Precision: Indicates the fraction of samples identified as positive by the model that are truly positive.

$$\text{Precision} = \frac{\text{True Positives}}{\text{True Positives} + \text{False Positives}} \tag{A15}$$

A high precision indicates that the model is making fewer false positive predictions, meaning it has a low rate of incorrectly classifying negative instances as positive. On the other hand, a low precision suggests that the model is making more false positive predictions, indicating that it may be less reliable in identifying positive instances.

- Recall: Measures the proportion of truly positive samples that the model successfully identifies as positive.

$$\text{Recall} = \frac{\text{True Positives}}{\text{True Positives} + \text{False Negatives}} \tag{A16}$$

A higher recall indicates that the model can correctly identify most true positive samples, while a lower recall suggests that the model may miss some true positive samples.

- F1-score: Represents the harmonic mean of precision and recall, offering a balanced assessment of the model's accuracy and completeness.

$$\text{F1} - \text{score} = \frac{2 \times \text{Precision} \times \text{Recall}}{\text{Precision} + \text{Recall}} \tag{A17}$$

The F1-score ranges from 0 to 1, with higher values indicating better model performance. It reaches its best value at 1 and worst value at 0.

- Confusion matrix for multiclass classification:
The confusion matrix for multiclass classification is a two-dimensional array. Each row represents a true class, and each column represents a predicted class. The elements on the diagonal of the matrix represent the number of samples correctly predicted by the model, while the other elements represent the number of incorrectly predicted samples.
- AUC-ROC curve:
The ROC curve for multiclass classification is a tool used to evaluate the performance of a multiclass classification model. It displays the classifier's performance across different classes by plotting the binary ROC curves for each class. The Area Under the ROC Curve (AUC) can be used to quantify the overall performance of the model.

References

1. Grant, A.O. Cardiac ion channels. *Circ. Arrhythmia. Electrophysiol.* **2009**, *2*, 185–194. [CrossRef] [PubMed]
2. Nerbonne, J.M.; Kass, R.S. Molecular physiology of cardiac repolarization. *Physiol. Rev.* **2005**, *85*, 1205–1253. [CrossRef]
3. Madhvani, R.V.; Xie, Y.; Pantazis, A.; Garfinkel, A.; Qu, Z.; Weiss, J.N.; Olcese, R. Shaping a new Ca^{2+} conductance to suppress early afterdepolarizations in cardiac myocytes. *J. Physiol.* **2011**, *589*, 6081–6092. [CrossRef]
4. Tomaselli, G.F.; Marban, E. Electrophysiological remodeling in hypertrophy and heart failure. *Cardiovasc. Res.* **1999**, *42*, 270–283. [CrossRef] [PubMed]

5. Weiss, J.N.; Garfinkel, A.; Karagueuzian, H.S.; Qu, Z.; Chen, P.S. Chaos and the transition to ventricular fibrillation: A new approach to antiarrhythmic drug evaluation. *Circulation* **1999**, *99*, 2819–2826. [CrossRef] [PubMed]
6. Zipes, D.P.; Wellens, H.J.J. Sudden cardiac death. *Circulation* **1998**, *98*, 2334–2351. [CrossRef]
7. Qiao, C.G.; Li, W.H.; Tang, G.N. Study on the effect of delayed recovery of extracellular potassium ion concentration on spiral wave. *Acta Phys. Sin.* **2014**, *23*, 238201. [CrossRef]
8. Sidorov, V.Y.; Woods, M.C.; Wikswo, J.P. Effects of elevated extracellular potassium on the stimulation mechanism of diastolic cardiac tissue. *Biophys. J.* **2003**, *84*, 3470–3479. [CrossRef]
9. Xiao, X.H.; Tang, G.N. Suppression of spiral waves and spatiotemporal chaos in cardiac tissue by elevating potassium ion concentration. *J. Biol. Eng.* **2012**, *29*, 29–34.
10. Shaw, R.M.; Rudy, Y. Electrophysiologic effects of acute myocardial ischemia: A theoretical study of altered cell excitability and action potential duration. *Cardiovasc. Res.* **1997**, *35*, 256–272. [CrossRef]
11. Luo, C.H.; Rudy, Y. A dynamic model of the cardiac ventricular action potential. I. Simulations of ionic currents and concentration changes. *Circ. Res.* **1994**, *74*, 1071–1096. [CrossRef]
12. Fujiu, K.; Nagai, R. Fibroblast-mediated pathways in cardiac hypertrophy. *J. Mol. Cell. Cardiol.* **2014**, *70*, 64–73. [CrossRef] [PubMed]
13. Gao, X.; Engel, T.; Carlson, B.E.; Wakatsuki, T. Computational modeling for cardiac safety pharmacology analysis: Contribution of fibroblasts. *J. Pharmacol. Toxicol. Methods* **2017**, *87*, 68–73. [CrossRef]
14. Xing, C.; Bao, L.; Li, W.; Fan, H. Progress on role of ion channels of cardiac fibroblasts in fibrosis. *Front. Physiol.* **2023**, *14*, 1138306. [CrossRef] [PubMed]
15. Munoz, V.; Campbell, K.; Shibayama, J. Fibroblasts: Modulating the rhythm of the heart. *J. Physiol.* **2008**, *586*, 2423–2424. [CrossRef]
16. Bazhutina, A.; Balakina-Vikulova, N.A.; Kursanov, A.; Solovyova, O.; Panfilov, A.; Katsnelson, L.B. Mathematical modelling of the mechano-electric coupling in the human cardiomyocyte electrically connected with fibroblasts. *Prog. Biophys. Mol. Biol.* **2021**, *159*, 46–57. [CrossRef] [PubMed]
17. Thompson, S.A.; Copeland, C.R.; Reich, D.H.; Tung, L. Mechanical coupling between myofibroblasts and cardiomyocytes slows electric conduction in fibrotic cell monolayers. *Circulation* **2011**, *123*, 2083–2093. [CrossRef] [PubMed]
18. Pellman, J.; Zhang, J.; Sheikh, F. Myocyte-fibroblast communication in cardiac fibrosis and arrhythmias: Mechanisms and model systems. *J. Mol. Cell. Cardiol.* **2016**, *94*, 22–31. [CrossRef]
19. Nayak, A.R.; Shajahan, T.K.; Panfilov, A.V.; Pandit, R. Spiral-wave dynamics in a mathematical model of human ventricular tissue with myocytes and fibroblasts. *PLoS ONE* **2013**, *8*, e72950. [CrossRef]
20. Mulimani, M.K.; Zimik, S.; Pandit, R. An in silico study of electrophysiological parameters that affect the spiral-wave frequency in mathematical models for cardiac tissue. *Front. Phys.* **2022**, *9*, 819873. [CrossRef]
21. Nguyen, T.P.; Xie, Y.; Garfinkel, A.; Qu, Z.; Weiss, J.N. Arrhythmogenic consequences of myofibroblast-myocyte coupling. *Cardiovasc. Res.* **2012**, *93*, 242–251. [CrossRef] [PubMed]
22. Peirlinck, M.; Costabal, F.S.; Yao, J.; Guccione, J.M.; Tripathy, S.; Wang, Y.; Ozturk, D.; Segars, P.; Morrison, T.M.; Levine, S.; et al. Precision medicine in human heart modeling: Perspectives, challenges, and opportunities. *Biomech. Model. Mechanobiol.* **2021**, *20*, 803–831. [CrossRef]
23. Shi, M.; Yu, H.; Wang, H. Automated detection of sudden cardiac death by discrete wavelet transform of electrocardiogram signal. *Symmetry* **2022**, *14*, 571. [CrossRef]
24. Pang, J.K.S.; Chia, S.; Zhang, J.; Szyniarowski, P.; Stewart, C.; Yang, H.; Chan, W.; Ng, S.Y.; Soh, B. Characterizing arrhythmia using machine learning analysis of Ca^{2+} cycling in human cardiomyocytes. *Stem Cell Rep.* **2022**, *17*, 1810–1823. [CrossRef]
25. Redkar, S.; Mondal, S.; Joseph, A.; Hareesha, K.S. A machine learning approach for drug-target interaction prediction using wrapper feature selection and class balancing. *Mol. Inf.* **2020**, *39*, 1900062. [CrossRef] [PubMed]
26. Lancaster, M.C.; Sobie, E. Improved prediction of drug-induced Torsades de Pointes through simulations of dynamics and machine learning algorithms. *Clin. Pharmacol. Ther.* **2016**, *100*, 371–379. [CrossRef]
27. Ahmed, A.A.; Ali, W.; Abdullah, T.A.A.; Malebary, S.J. Classifying cardiac arrhythmia from ecg signal using 1D CNN deep learning model. *Mathematics* **2023**, *11*, 562. [CrossRef]
28. Song, E.; Lee, Y.S. Interpretable machine leaning of action potential duration restitution kinetics in single-cell models of atrial cardiomyocytes. *J. Electrocardiol.* **2022**, *74*, 137–145. [CrossRef] [PubMed]
29. Grandits, T.; Augustin, C.M.; Haase, G.; Jost, N.; Mirams, G.R.; Niederer, S.A.; Plank, G.; Varro, A.; Virag, L.; Jung, A. Neural network emulation of the human ventricular cardiomyocyte action potential for more efficient computations in pharmacological studies. *eLife* **2024**, *12*, RP91911. [CrossRef]
30. Trayanova, N.A.; Popescu, D.M.; Shade, J.K. Machine learning in arrhythmia and electrophysiology. *Circ. Res.* **2021**, *128*, 544–566. [CrossRef]
31. Jeong, D.U.; Lim, K.M. Prediction of cardiac mechanical performance from electrical features during ventricular tachyarrhythmia simulation using machine learning algorithms. *Front. Physiol.* **2020**, *11*, 591681. [CrossRef] [PubMed]
32. Christoph, J.; Lebert, J. Inverse mechano-electrical reconstruction of cardiac excitation wave patterns from mechanical deformation using deep learning. *Chaos* **2020**, *30*, 123134. [CrossRef]

33. Mulimani, M.K.; Alageshan, J.K.; Pandit, R. Deep-learning-assisted detection and termination of spiral and broken-spiral waves in mathematical models for cardiac tissue. *Phys. Rev. Res.* **2020**, *2*, 023155. [CrossRef]
34. Jeong, D.U.; Lim, K.M. Artificial neural network model for predicting changes in ion channel conductance based on cardiac action potential shapes generated via simulation. *Sci. Rep.* **2021**, *11*, 7831. [CrossRef] [PubMed]
35. Ten Tusscher, K.H.W.J.; Noble, D.; Noble, P.J.; Panfilov, A.V. A model for human ventricular tissue. *Am. J. Physiol. Heart Circ. Physiol.* **2004**, *286*, H1573–H1589. [CrossRef]
36. Davidenko, J.M.; Pertsov, A.V.; Salomonsz, R.; Baxter, W.; Jalife, J. Stationary and drifting spiral waves of excitation in isolated cardiac muscle. *Nature* **1992**, *355*, 349–351. [CrossRef]
37. Luo, C.H.; Rudy, Y. A model of the ventricular cardiac action potential depolarization, repolarization, and their interaction. *Circ. Res.* **1991**, *68*, 1501–1526. [CrossRef]
38. Xie, Y.; Garfinkel, A.; Weiss, J.N.; Qu, Z. Cardiac alternans induced by fibroblast-myocyte coupling: Mechanistic insights from computational models. *Am. J. Physiol. Heart Circ. Physiol.* **2009**, *297*, H775–H784. [CrossRef] [PubMed]
39. Camelliti, P.; Green, C.R.; Kohl, P. Structural and functional coupling of cardiac myocytes and fibroblasts. *Cardiovasc. Gap Junctions* **2006**, *42*, 132–149.
40. Jacquemet, V.; Henriquez, C.S. Loading effect of fibroblast-myocyte coupling on resting potential, impulse propagation and repolarization: Insights from a microstructure model. *Am. J. Physiol. Heart Circ. Physiol.* **2008**, *294*, H2040–H2052. [CrossRef] [PubMed]
41. Jacquemet, V. Pacemaker activity resulting from the coupling with nonexcitable cells. *Phys. Rev. E* **2006**, *74*, 011908. [CrossRef] [PubMed]

Disclaimer/Publisher's Note: The statements, opinions and data contained in all publications are solely those of the individual author(s) and contributor(s) and not of MDPI and/or the editor(s). MDPI and/or the editor(s) disclaim responsibility for any injury to people or property resulting from any ideas, methods, instructions or products referred to in the content.